Contactless RF Probe Interconnect Technology Enabling Broadband Testing to the Terahertz Range

Alejandro Rivera-Lavado, Muhsin Ali, Daniel Gallego-Cabo, Luis-Enrique García-Muñoz, Dmitri V. Lioubtchenko, *Member, IEEE*, and Guillermo Carpintero, *Senior Member, IEEE*

***Abstract*—Radiofrequency (RF) probes based on 50-Ω planar transmission lines play a key role in almost every stage of RF device development, establishing the physical contact between high-end instrumentation and the device. With the continuous downscaling of semiconductor technologies to reach into the millimeter-wave (30–300 GHz) and Terahertz (300 GHz to 3 THz) bands and devices exhibiting broader frequency response, current RF probe technology is the Achilles heel for precise and repeatable measurements. Here, we propose a novel RF probe technology based on the near-field coupling of single-mode dielectric waveguide structures, which according to our full-wave simulations provide an extremely broad frequency range covering from 0 Hz up to 340 GHz, the largest continuous bandwidth reported to date. A concept demonstrator using this approach shows contactless RF probing on test structures, which shows the path toward continuous measurements across the microwave, millimeter-wave, and Terahertz range.**

***Index Terms*—Contactless probe, dielectric rod waveguide (DRW), terahertz, ultra-wideband interconnection.**

I. Introduction

THE frequency bands above 100 GHz have unique characteristics, such as penetration through fog, rain, and cloud, which are attractive in a variety of applications, being the vast amounts of available bandwidth a key characteristic for ultra-high-speed wireless and satellite communications [1]. Different bands have recently been allocated above 100 GHz for commercial telecommunication services in Japan (116–134 GHz) and United States (116–123 GHz, 174.8–182 GHz, 185–190 GHz, and 244–246 GHz) [2]. To reach these bands, the electronics industry has evolved through a continuous downscaling of semiconductor technologies to unlock higher cut-off frequencies [3]. State-of-the-art Monolithic Integrated Circuits (MMIC) using metamorphic High Electron Mobility Transistor (mHEMT) technology reached above 500 GHz [4] while high-speed photodiodes used in microwave photonics reached above 2 THz [5], [6].

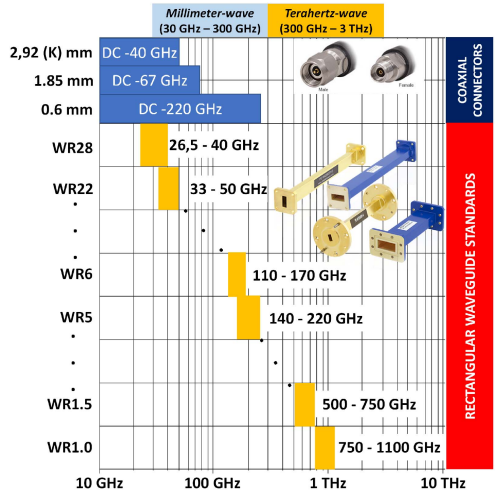

Fig. 1. Frequency range of coaxial and rectangular waveguide standardized interconnection interfaces covering the millimeter- and Terahertz wave ranges of the spectrum.

Radiofrequency (RF) probes play a key role in almost every step of the RF devices lifecycle, enabling measuring the true characteristics of the RF components at the chip level. RF probes were initially developed by Tektronix in the 1980s and have evolved with an exponential increase in their maximum frequency [7]. Although frequencies up to 1.1 THz are feasible [8], the maximum frequency is usually limited by the connector interfacing the RF probe to the test equipment. Standardized coaxial connectors provide a continuous operating frequency range from dc (0 Hz) up to a maximum frequency determined by the connector type: 40 GHz for the 2.92 mm (K) connector, 67 GHz for the 1.85-mm connector and, more recently, 110 GHz with the 1-mm connector [9], and 220 GHz for the 0.6 mm one (see Fig. 1). For frequencies above 220 GHz, the dimensions of coaxial become impractically small and rectangular waveguide interconnects become the only option. These allow interconnects

Manuscript received 11 April 2022; revised 18 August 2022, 21 September 2022, and 4 October 2022; accepted 4 October 2022. Date of publication 10 October 2022; date of current version 18 January 2023. This work was supported by the European Union's Horizon 2020 Research and Innovation Program under Grant 862788 (TERAmeasure FET Open project). *(Corresponding author: Alejandro Rivera-Lavado.)*

Alejandro Rivera-Lavado is with the Departamento de Teoría de la Señal y Comunicaciones, Leganés, Universidad Carlos III de Madrid, 28911 Leganes, Spain, and also with the Dirección General del Instituto Geográfico Nacional, Yebes Observatory, 19141 Yebes, Spain (e-mail: arivera@ing.uc3m.es).

Muhsin Ali, Daniel Gallego-Cabo, and Guillermo Carpintero are with the Departamento de Tecnología Electrónica, Leganés, Universidad Carlos III de Madrid, 28911 Madrid, Spain (e-mail: muali@ing.uc3m.es; dcgallego@ing.uc3m.es; guiller@ing.uc3m.es).

Luis-Enrique García-Muñoz is with the Departamento de Teoría de la Señal y Comunicaciones, Leganés, Madrid, Universidad Carlos III de Madrid, 28911 Madrid, Spain (e-mail: legarcia@ing.uc3m.es).

Dmitri V. Lioubtchenko is with the Department of Micro and Nano Science, KTH Royal Institute of Technology, 10044 Stockholm, Sweden (e-mail: dml@kth.se).

Color versions of one or more figures in this article are available at https://doi.org/10.1109/TTHZ.2022.3213470.

Digital Object Identifier 10.1109/TTHZ.2022.3213470

up to 1.1 THz, with the important drawback of being band limited [10], as shown in Fig. 1.

On the other RF probe end, the interface between the probe and the device under test (DUT) is established through termination of a 50-Ω RF planar transmission line defining the probe tip. Designed to maintain the 50-Ω condition as close as possible to the DUT pads [7]. The contact pad structure depends on the type of transmission line (Co-Planar Waveguide, Co-Planar Stripe,...) used in the DUT, which established different arrangements for the signal and ground contacts, which must be reproduced by the probe tip. The RF probe must land the probe tip contacts onto the corresponding DUT pads to achieve an electrical connection at this interface. As frequency increases, the spacing between the pads decreases down to 25 μm [8], making this approach extremely challenging. Accurate and repeatable measurements between 500 GHz require probe placement errors below 1 μm, beyond manual positioning capabilities, to achieve a phase uncertainty smaller than 1° [11] and to avoid the excitation of parasitic higher-order modes, which alter the DUT frequency response as well as degrade the accuracy of the calibration [12]. Another critical issue for measuring device characteristics on-chip is probe crosstalk, from probe-to-probe signal coupling [13] and probe coupling with neighboring structures [14]. In addition, the physical nature of the contact introduces sensitiveness to temperature variations and vibrations, causing uncertainties over long measurement periods, and also causing wear of the probe tip limiting the number of possible measurements. It has been noted that improving on-chip high-frequency measurements require the correct design of RF probes [15], which have become the Achilles heel for precise and repeatable measurements at millimeter- and Terahertz wave ranges.

Noncontact RF probing is a desirable feature aiming for more stable, more repeatable measurements. Several solutions have been reported to date. One approach is based on defining planar antennas at each DUT access port, using a quasi-optical electromagnetic coupling requiring parabolic mirrors and placing the DUT onto a hemispherical silicon lens to feed the signals from vector network analyzer (VNA) extension heads [16]. This approach has all the drawbacks of using rectangular waveguide coupled extension heads, which are band limited and prevent from providing measurements across the entire spectrum. A different approach employs dielectric waveguide structures to achieve high-frequency probes. A simple dielectric probe operating in the sub-terahertz band from 190 to 220 GHz is based on a silicon dielectric tip coupling the electromagnetic energy from a high-resistive silicon dielectric waveguide (SDW) into another dielectric waveguide on a substrate [17]. This solution requires the wave to undergo multiple reflections along the coupling tip to achieve the critical angle and couple into the dielectric waveguide, being the source of its high losses. A more recent noncontact probing scheme using dielectric waveguides has demonstrated, using a dielectric rod waveguide (DRW) and a coplanar waveguide (CPW), operating over the range from 50 to 75 GHz, with 1.6-dB insertion loss and −20 dB return loss at 65 GHz [18]. However, all the current dielectric waveguide-based probing solutions reported to date excite the dielectric waveguide through inserting them into metallic rectangular waveguides, which again limits the operating frequency range to that of the used WR flange (190–260 -WR5.1- in [17] and 50–75 GHz -WR15- in [18]).

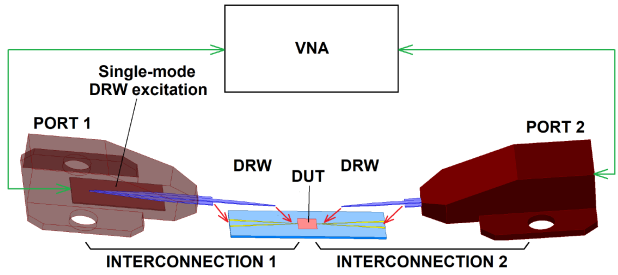

Fig. 2. Sketch of a 2-port DUT measurement setup. Two dielectric probes are used for obtaining the 2 × 2 S-parameter matrix.

We present a new RF probing concept [19] that relies on a novel broadband single-mode excitation scheme of dielectric waveguide structures, in the present work, a DRW [20], [21], [22], demonstrating the proof-of-principle for a noncontact probe operating over multiple WR bands. This novel RF probe approach uses near-field coupling to the DRW, which eliminates the need for physical contact and enables contactless operation. In addition, the near-field coupler is designed to excite only one DRW mode over a wide frequency range, allowing to achieve the largest continuous bandwidth reported to date ranging from 0 Hz to above 340 GHz. In summary, we present a novel RF probing paradigm based on dielectric waveguides that unlocks desirable characteristics such as noncontact operation over a broad frequency range with a single probe.

II. High-Frequency Contactless Dielectric Interconnection Structure

A. Description

The core of the RF probe uses a novel high-frequency contactless RF interconnect concept based on dielectric waveguides. Fig. 2 shows a 2-port measurement setup. The complete characterization of the DUT is achieved with two ultra-broadband interconnections, 1 and 2. In this section, we describe this novel interconnect concept. Sections III and IV demonstrate the feasibility of this approach with simulations and measurement results. Due to the achieved bandwidth, it is especially convenient for photonic-driven VNAs, where a photomixer source, two photoconductive receivers, and a ultra-broadband directional coupler per port allow the measurement of the incident and reflected wave phase and amplitude. A further discussion of this is out of the scope of this article. This article is focused on the contactless interconnection and the single-mode excitation of the dielectric structure.

Our approach to achieve a high-frequency contactless interconnect, shown in Fig. 3(a), is based on the combination of coplanar antennas and dielectric waveguide structures. Fig. 3(a) sketches a single interconnection between two generic RF ports, RF Port A from Device A with RF port B from Device B. In this particular application, Device A corresponds to the single-mode

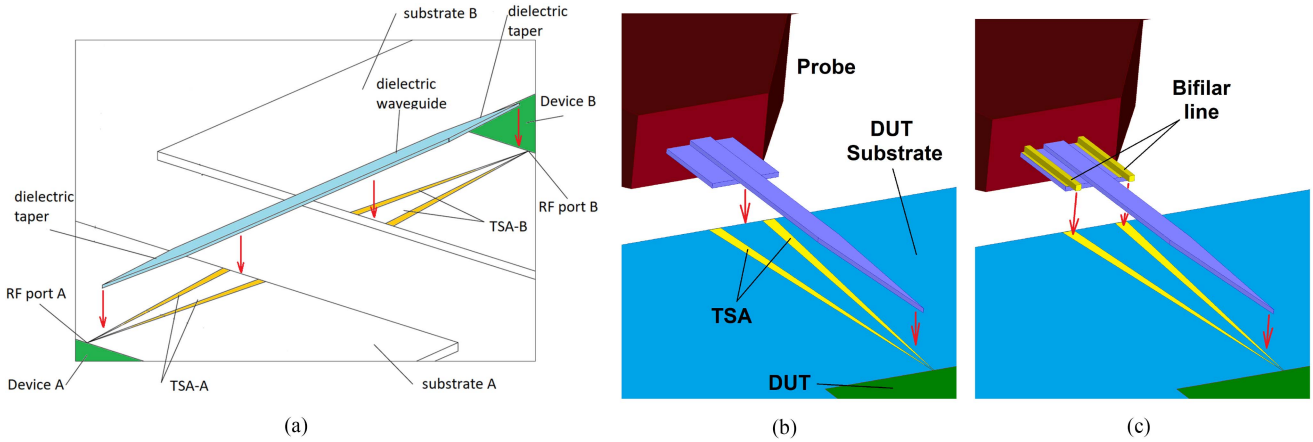

Fig. 3. Ultra-wideband interconnection structure. A high-permittivity DRW is placed over two coplanar antennas (TSA-A and TSA-B). (a) If the distance between the DRW and the TSAs substrates is low enough (see Section III), a signal link is established between the devices A and B. (b) Same structure implementing a test probe that is landing to a DUT. (c) If two contact metal pins (dark yellow) are added, the probe range can be extended up to dc (see Section B).

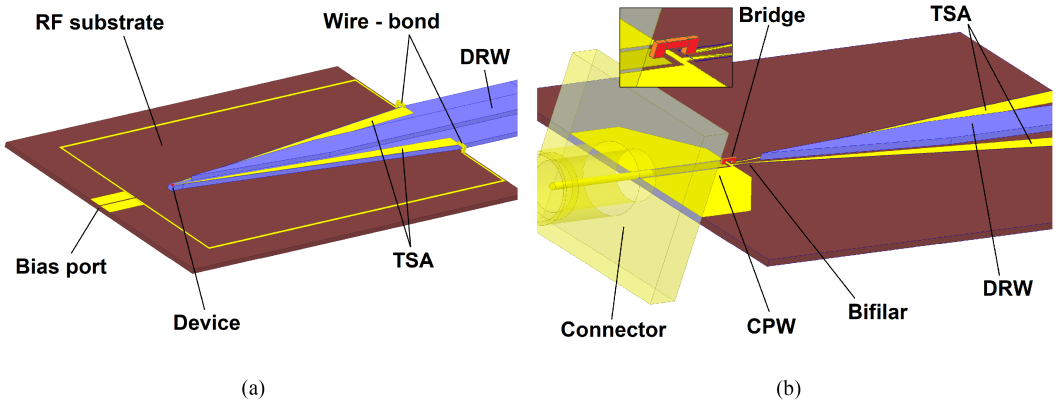

Fig. 4. Excitation of the TSA mode launcher: (a) By using an integrated electronic or optoelectronic device with a high impedance dc bias interconnection and (b) by using a coaxial connector and a CPW-to-CPS transition. The inset shows the CPW-to-CPS metal bridge (red) that connects the central strip of the CPW line (dark yellow) with one of the TSA arms.

excitation of the DRW, and device B is the DUT port. The interconnection is established through a DRW structure made of the high-permittivity material, bridging the RF signals between the two ports. The RF signals are launched at one port, propagate through the DRW, coupling from the DRW to the opposite port. The interconnection concept used as a test probe is shown in Fig. 3(b). Its contactless capabilities are demonstrated with S_{21} measurements for different gaps ΔZ between the DRW and the DUT substrate from 55 to 110 GHz using the manufactured coaxial connector-based proof-of-concept. The DRW width of the probe W_{DRW} defines a low cutoff frequency (f_{LCO}). The frequency range can be extended up to dc if two metal contacts are added [see Fig. 3(c)]. Such metal contacts are intended to work from dc to the dielectric structure with low cutoff frequency. Because of this, a proper selection of that cutoff frequency leads to alignment tolerances less restrictive than the ones with GSG probes. In this dc extension, only the metal strips require contact. The dielectric probe, the most sensible part of the probe, can still work contactless.

The key to our approach is that the RF signals at each port are launched into the DRW exciting only a single mode using: 1) linear-tapered slot antenna (TSA) and 2) tapered ends of the dielectric waveguide. Both ensure a smooth transition of the characteristic impedance Z_0 between the TSA and the DRW. The excitation of the TSA is done through the balanced bifilar line composed of the two TSA arms. In addition, the TSA length is greater than dielectric waveguide taper length to avoid signal reflections at the TSA termination. This structure can be directly grown instead of the current contact pads of advanced RF MMICs as well as optoelectronic sources, such as photoconductive [23], UTC [24], or *n-i-pn-i-p* [25] photodiodes. In this configuration [see Fig. 4(a)], it is possible to bias the device with metal tracks (yellow) printed in a low-permittivity substrate, such as Rogers RT/Duroid 5880 (brown). This configuration allows us to take advantage of the ultra-broadband of sources and detectors. We choose this configuration to demonstrate the wideband response from 55 to 340 GHz (see Fig. 5) and from 0 Hz to 340 GHz (see Fig. 6) with full-wave simulations (see Section B). The higher frequency of our analysis is limited by the available computational resources. Fig. 4(b) shows an alternative excitation, on which a coaxial connector and a CPW-to-CPS transition [26] are used to feed the TSA. We choose this

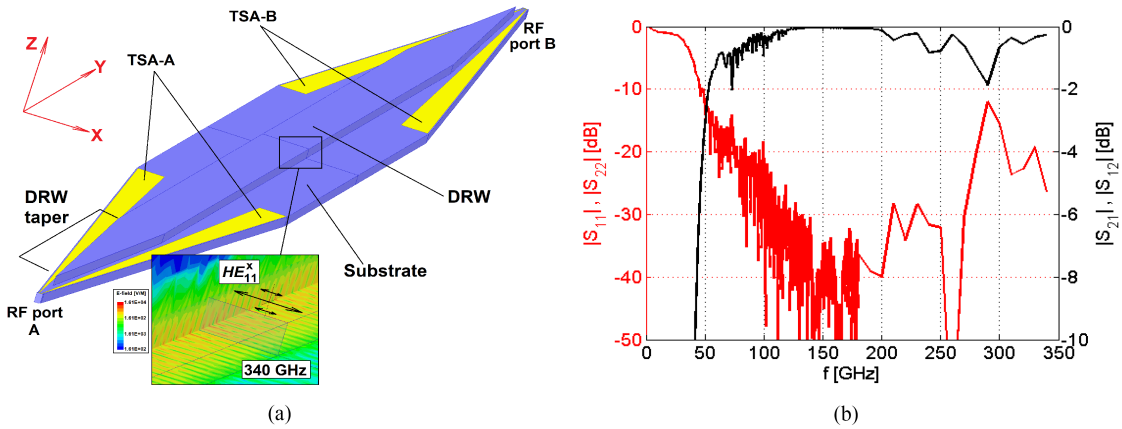

(a) (b)

Fig. 5. (a) Simulation model of the high-frequency interconnection structure combining coplanar antennas and dielectric waveguide, and (b) simulated scattering parameters (S_{11}, S_{22}, red; S_{21}, S_{12}, black) representing the frequency response, starting at $f_{\mathrm{LCO}} = 55$ GHz and reaching into the Terahertz range beyond 350 GHz.

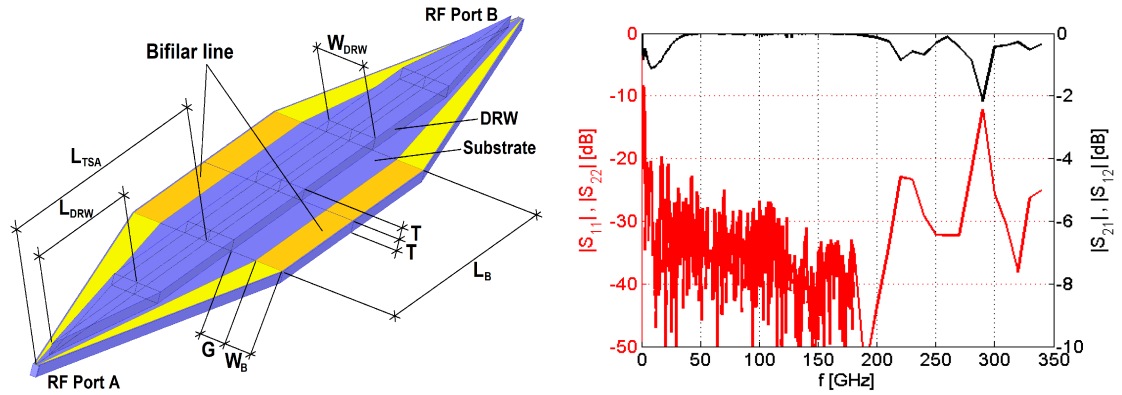

(a) (b)

Fig. 6. (a) Simulation model of the high-frequency interconnection structure combining coplanar antennas and dielectric waveguide, and (b) simulated scattering parameters (S_{11}, S_{22}, red; S_{21}, S_{12}, black) representing the frequency response, ranging from dc to beyond 350 GHz.

configuration (using a 1-mm connector) to interface with our Anritsu VNA in the experimental demonstration (see Section C). These connectors not only limit the maximum frequency to 110 GHz but also introduce attenuation roll-off that the simulation does not include. For these reasons, while the traces are not one-to-one comparable, the simulation allows us to demonstrate the wide bandwidth and single-mode excitation of the dielectric waveguide. On the other hand, the experimental results demonstrate the consistent low-frequency roll-off and the noncontact interconnect characteristic.

The high-frequency DRW is bidirectional and presents a high-pass frequency response, which is determined by the TSA (the DRW structure does not have an abrupt low cut-off limit [21]). Only signals with frequencies above a low cut-off frequency f_{LCO}, which depends on the DRW width $\mathrm{W_{DRW}}$ and the ratio between the length of the TSA to the length of the dielectric waveguide taper ($L_{\mathrm{TSA}}/L_{\mathrm{DRW}}$), are coupled to the DRW. Increasing this ratio is possible to reduce f_{LCO} without increasing the DRW width. The dielectric structure couples high-frequency signals via a near-field coupling, so there is no need for physical contact between the dielectric tip and the device substrate to achieve low loss. As we will show, it is possible to extend the frequency response toward lower frequencies by incorporating metallic extensions to the TSA arms, creating a bifilar line interconnecting the two ports TSA tips.

It is a known fact that dielectric waveguides are a dispersive propagation media. However, for high-frequency characterization and test of devices, this is not an issue, as we commonly use a single tone whose frequency is swept over the frequency range of interest. A calibration step allows us to compensate the dielectric waveguide dispersion in the signal phase. The advantage of our approach is that most of the power is coupled in a single mode, which leads to a predominant signal path through the structure, so intermodal interference is avoided. When the TSA matches the DRW taper, the bandwidth is extended to frequencies above the cut-off frequency of DRW higher-order modes. Ours is a novel approach that differs from other similar structures [27] that achieve smaller bandwidths.

B. Design Results

To demonstrate the characteristics of the novel high-frequency contactless RF interconnect structure, standard numerical simulation software has been used to solve for the frequency response

when used to interconnect RF Port A with RF port B, as shown in Fig. 3, demonstrating that enables an operating frequency range above 340 GHz. All simulations were done using the full-wave simulator ANSYS HFSS [28] from 10 MHz to 340 GHz in 12 different subbands. From 10 MHz to 1 GHz, the frequency step is 4.4 MHz, from 1 to 180 GHz is 250 MHz, and from 180 to 340 GHz is 10 GHz. A mesh refinement with a maximum elements length of 3 μm in the vertex of the TSA metallization is required for achieving consistency between results of the different subbands. At low frequencies, the default meshing options lead to inconsistent results. 64 GB of RAM is required for simulating the structure up to 340 GHz. Both metal and dielectric are assumed to be lossless.

The dielectric waveguide structure with the coupling TSA antennas is shown in Fig. 5(a). For the simulation, we have assumed a DRW made of low-loss high-resistive silicon, with thickness $T = 200$ μm. As the worst scenario, the simulation structure assumes a high-permittivity material (high-resistive silicon) substrate on which the TSA antennas are grown, shown in Fig. 5(a) as yellow metal patterns. The single-mode excitation of the DRW is achieved by the TSA and the DRW taper. The total length of the TSA is $L_{\text{TSA}} = 14.5$ mm and a width of 3 mm. The TSA metal is tapered from 10 μm at the RF port tip to 0.54 mm at the TSA termination end. The TSA gap is also tapered, from 50 μm at the RF port to 1.93 mm at the termination. For this TSA, we have selected a DRW taper length of $L_{\text{DRW}} = 7.25$ mm, which ensures a smooth characteristic impedance Z_0 transition between the port bifilar line and the DRW. When assuming a silicon relative permittivity ε_{r} of 11.9, a metal strip width of 10 μm, and a gap of 50 μm, a characteristic impedance Z_0 of 160 Ω is obtained via full-wave simulations. For 50-Ω integrated devices, extra broadband and transitions to other transmission line technology may be required, while for optoelectronics devices, better impedance matching can be achieved by increasing the TSA tip Z_0. The inset shows the simulated E-field amplitude distribution at 340 GHz. Since only the mode excited by the TSA is present (HE_{11}^x) there is no intermodal interference, and the signal propagation occurs without nulls over the studied frequency range. This mode is in the same orientation as the TSA polarization, which ensures an efficient signal coupling between TSA and DRW.

The simulated S-parameter of the dielectric waveguide interconnect structure is shown in Fig. 5(b). The result shows that this structure efficiently couples signals between the two RF ports with a low cut-off frequency $f_{\text{LCO}} = 55$ GHz. The operating frequency range extends from f_{LCO} to, at least, 340 GHz with a 6-dB insertion losses criterion for a back-to-back configuration. For frequencies above 60 GHz, the reflection losses (RLs) are greater than 15 dB, and the back-to-back insertion losses are lower than 2 dB.

We have also simulated the response of the structure including the metallic bifilar line to extend the frequency response toward the lower frequencies, removing the lower cut-off frequency f_{LCO}. To the previous structure, we include a bifilar line connecting the tapered terminations of the TSA antennas. The resulting structure is shown in Fig. 6(a), in which the bifilar line has been added to the dielectric structure, highlighted in orange color. The

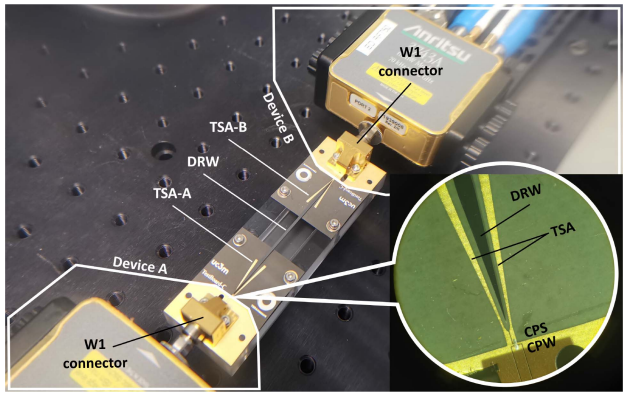

Fig. 7. Assembled back-to-back proof of concept using 1-mm coaxial connectors to interface with the TSA antennas using a CPW-to-CPS transition. The inset represents the transition from the W1 coaxial connector with the CPW interface with the TSA antenna CPS feed.

bifilar strip width is 0.54 mm and the separation between the DRW and the bifilar line is 500 μm, selected to avoid the bifilar line disrupting the DRW single-mode transmission for signals with frequencies above f_{LCO}, when the signal energy is confined within the high-permittivity DRW structure. Actually, the E-field is parallel to the X-axis (HE_{11}^x). The evanescent signal power outside the DRW is not negligible at low frequencies ($f < f_{\text{LCO}}$). The fields are arranged in a TEM mode between the two metallic wires, confirmed via full-wave simulations. The structure including the bifilar line achieves insertion losses below 2.1 dB from 0 Hz to 340 GHz for a distance between the two TSAs of 12 mm. RLs are typically greater than 20 dB. The worst value is found at 1.5 GHz (RL = 8.27 dB), in a resonance related to the distance between ports.

C. Experimental Results

To demonstrate the novel interconnect concept, we have developed an experimental back-to-back proof-of-concept demonstrator of the ultra-wideband interconnection structure shown in Fig. 3(a). A photograph of the test structure, placed within the measurement setup, is shown in Fig. 7. The figure shows how the devices, Device A and Device B, are composed of an Anritsu 3743 A millimeter-wave broadband extension head with an operating frequency range from 70 kHz to 110 GHz, a coaxial 1-mm PCB connector and a CPW to coplanar stripe (CPS) transition. These feed each port high-frequency contactless RF interconnect coplanar TSA antenna. The substrate on which the coaxial 1-mm PCB connector, the transition, and the TSA antenna were fabricated is a low-permittivity material, Rogers RT/Duroid 5880.

Two of these assemblies are connected to the RF ports of the Anritsu 3743 A millimeter-wave broadband extension heads, and a DRW is used to interconnect both assemblies, as shown in Fig. 7. The DRW uses low-losses high-resistivity undoped silicon of 500 μm thickness. We experimentally measure the S-parameters of the structure with an Anritsu MS4647B VNA. Each frequency swept has 10.001 points, linearly distributed from 70 kHz to 110 GHz. The VNA intermediate frequency

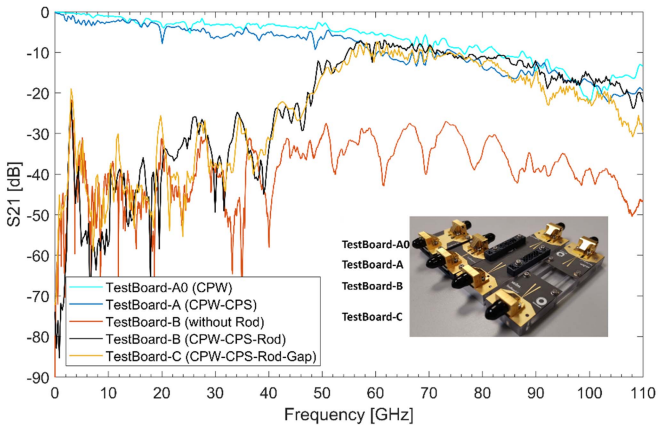

Fig. 8. Measured transmission coefficients S_{21} of the different test board structures, feed by W1-coaxial connectors.

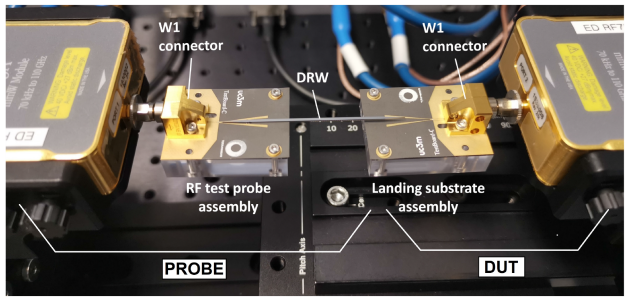

Fig. 9. Assembled RF test probe demonstrator placing two TestBoard-C structures on independent methacrylate base plates, gluing the DRW structure to one of the substrates (left). The structures were fixed through the W1-coaxial connectors to the Anritsu 3743 A millimeter-wave broadband extension heads, which were placed onto positioning stages with five degrees of freedom.

(IF) bandwidth is set to 1 kHz. To isolate the effects introduced by the 1-mm connectors and the CPW to CPS transitions, four different test boards have been fabricated as references, shown in the inset of Fig. 8.

1) TestBoard-A0: The two RF port 1-mm connectors were connected with a CPW line. This test board established the baseline for the frequency response of the interconnect.
2) TestBoard-A: The two RF port 1-mm connectors CPW line was followed by a CPW-to-CPS transition, connecting both ports through a CPS bifilar line. This test board allows us to evaluate the influence of the transition required for the TSA antennas.
3) TestBoard-B: Each 1-mm connector was followed by a CPW line, a CPW-to-CPS transition, and a TSA antenna, all of which are on a single substrate.
4) TestBoard-C: Two different substrates were used for each RF port, providing a W1-connector followed by a CPW line, a CPW-to-CPS transition, and TSA antenna.

To interconnect the RF port TSA antennas in TestBoard-B and TestBoard-C, we manufactured a DRW with 1 mm width ($W_{\mathrm{DRW}} = 1$ mm), 0.5 mm thickness ($T = 0.5$ mm), and 8-mm taper length. The distance between TSA antennas L_{B} is 31.4 mm. TSA length is $L_{\mathrm{TSA}} = 15.0$ mm, G is 1.0 mm, and W_{B} is 1.0 mm. The test boards were mounted on methacrylate base plates for structural rigidity and measured with the Anritsu MS4647B VNA.

The measured transmission coefficient S_{21} for each of the TestBoard structures is shown in Fig. 8. The light blue line is the result for TestBoard-A0, in which the two W1-connectors were connected with the CPW specified by the manufacturer and serves as the reference. The manufacturer specifies the insertion losses in a similar structure on the order of -0.489 dB at 10 GHz, -2.693 dB at 90 GHz, and -7.117 at 110 GHz with a Rogers RO3003 substrate [29]. Our TestBoard-A0 provides similar results with a Rogers RT/Duroid 5880. The introduction of the CPW-to-CPS transition does not significantly alter these results, as observed in Fig. 8. It is also clearly observed that the novel structures that we proposed exhibit a low cut-off frequency (f_{LCO}). Due to the low relative permittivity ($\varepsilon_{\mathrm{r}} = 2.2$) of the Rogers RT/Duroid 5880 substrate, f_{LCO} increased from the designed 45 GHz achieved in simulation to 55 GHz. For frequencies above 55 GHz, the insertion losses are similar, so the performance of our solution is similar to the bifilar line. The absence of transmission nulls between 55 and 110 GHz implies a lack of internal reflections inside the proof-of-concept, so a good matching is achieved between the bifilar line, the TSA pad, and the DRW. Furthermore, it means that there is no coexistence of two or more propagating modes inside the rod since there are no signs of intermodal interference in S_{21}. To prove that the transmission is done through the DRW, S_{21} without the dielectric waveguide is provided for the TestBoard-B prototype (red). As expected, since the TSA pads act as antennas, there is still transmission, but an extra loss factor of 30 dB is added to the link. Furthermore, we observe an interference pattern in the working band, with a mean free spectral range (FSR) $\Delta\nu_{\mathrm{FSR}} = 7.96$ GHz. It is defined as $\Delta\nu_{\mathrm{FSR}} = c/(n_{\mathrm{g}} L_{\mathrm{R}})$, where c is the speed of light in vacuum, n_{g} is the refractive index. When considering air ($n_{\mathrm{g}} = n_0 = 1$), it leads to a resonance length L_{R} of 37.7 mm, close to the distance between TSA antennas. This allows us to establish that there are signal reflections between them.

III. High-Frequency Contactless Dielectric RF Probe

A. Description

In this section, we introduce our novel high-frequency RF probe concept, based on the high-frequency interconnect that we have described above. To develop the RF test probe, we use one of the TestBoard-C substrates that include a W1-connector, followed by a CPW line, a CPW-to-CPS transition, and TSA antenna. The DRW is then glued on the Rogers RT/Duroid 5880, carefully placing it in its optimum position, symmetrically with respect to the TSA pads. Another structure is assembled as a landing substrate, including the W1-connector and Rogers RT/Duroid 5880 with the CPW line, CPW-to-CPS transition, and the TSA antenna. Both are placed on independent methacrylate base plates, using the W1-coaxial connectors to attach each assembly to an Anritsu 3743 A millimeter-wave broadband extension head, as shown in Fig. 9. Each broadband extension head was mounted on positioning stages providing five degrees

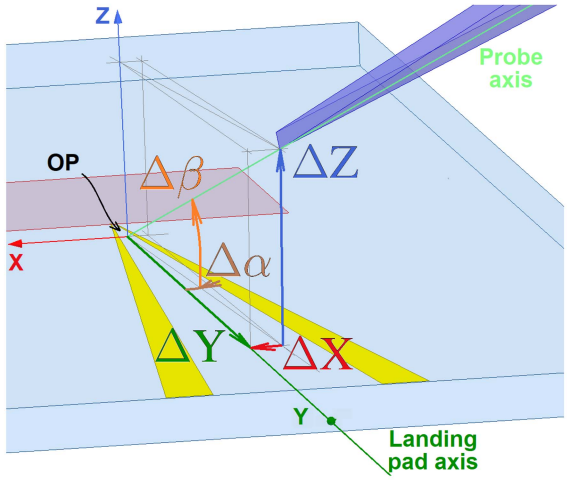

(a)

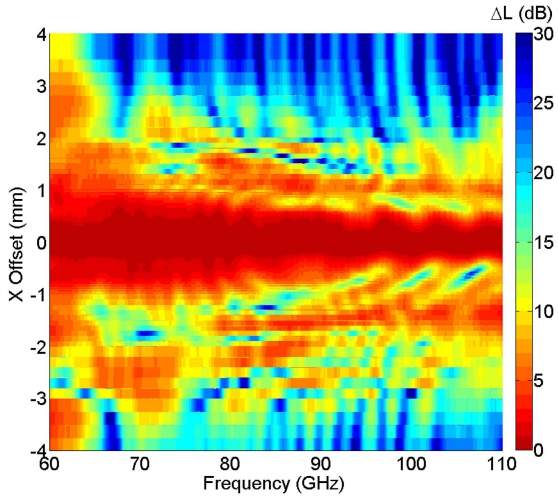

(b)

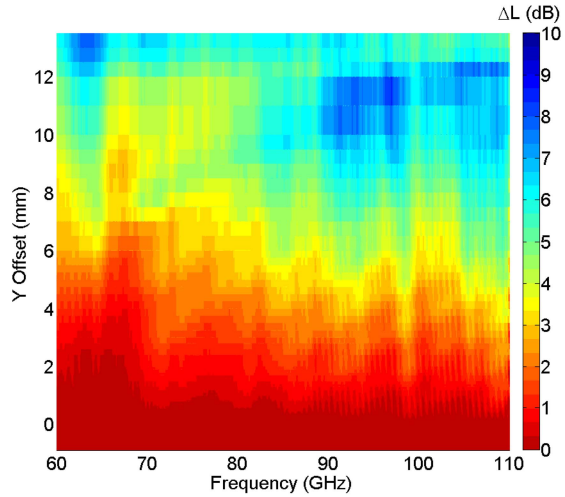

(c)

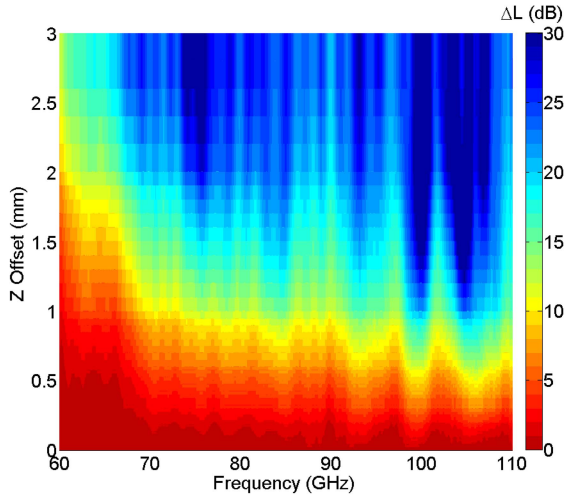

(d)

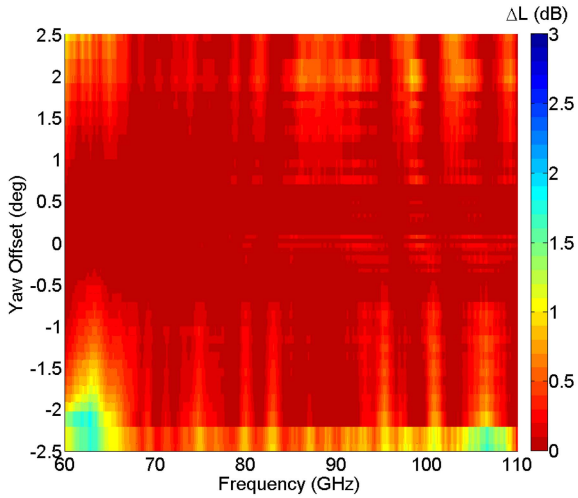

(e)

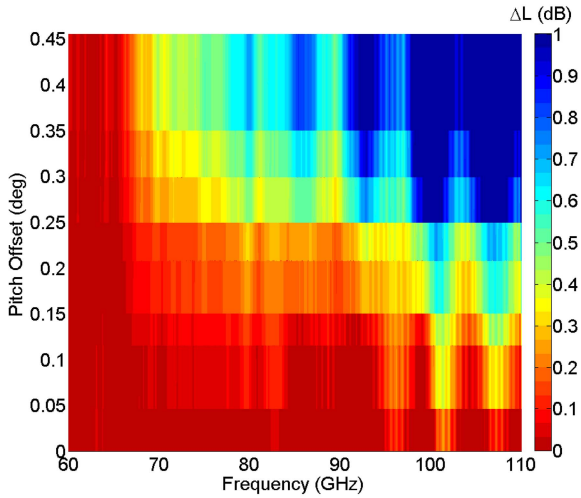

(f)

Fig. 10. Alignment tolerances study. (a) Error definitions for a probe (purple) landing in a 1-port DUT. Attenuation ΔL in decibels is shown for frequencies between 60 and 110 GHz and for an alignment error in the (b) X-axis (ΔX), (c) Y-axis (ΔY), (d) Z-axis (ΔZ), (e) the yaw angle ($\Delta\alpha$), and (f) the pitch angle ($\Delta\beta$).

of freedom between the two structures, to analyze the influence of the alignment between them on the high-frequency interconnection performance.

B. Accuracy of Alignment Requirements

We performed a study of the alignment error tolerances with the setup shown in Fig. 9. The optimum DRW position is determined by full-wave simulations of the back-to-back model. We have defined the optimum in terms of insertion losses, planarity of S_{21}, and maximum working frequency in a single-mode working regime. The experimental setup allows testing errors in the X, Y, and Z axes, as well as two angular errors (pitch and yaw), as shown in Fig. 10(a). The offsets for each axis are defined with respect to the coordinate origin placed at the optimum DRW tip position (OP), being positive in the direction shown for each one (ΔX, ΔY, ΔZ, $\Delta\alpha$, and $\Delta\beta$). All measurements were normalized with respect to the measured response at this optimum placement of the DRW, representing the response as the additional attenuation introduced by the offset for each axis. We introduce the additional attenuation factor ΔL obtained for frequencies between 60 and 110 GHz with a frequency step of 11 MHz.

Our measurements, shown in Fig. 10(b)–(f) for the offset errors ΔX, ΔY, ΔZ, $\Delta\alpha$, and $\Delta\beta$, respectively, highlight that our interconnection solution is robust again spatial alignment errors. It is possible to ensure a connection loss ΔL lower than 1 dB for frequencies up to 110 GHz if the alignment error is smaller than 100 μm. In the X-axis, there is signal transmission when the DRW lies inside the arms of the landing pad TSA metallic pattern. For the Y-axis, an error of ± 700 μm around the optimum landing site ensures a $\Delta L < 1$ dB. Testing Y-offsets lower than -0.8 mm was not possible in our setup since the DRW can damage the bridge of the CPW-to-CPS transition [26].

A key aspect is that, as shown in Fig. 10(d), it is possible to achieve efficient signal coupling without physical contact along with the measured bandwidth. A 40-μm gap between the DRW probe and the landing TSA ensures a transmission loss $\Delta L < 1$ dB up to 110 GHz. If a $\Delta L < 3$ dB is acceptable, then a gap of 150 μm is allowed. According to our study, the probe is robust to angular error. Up to 110 GHz, a yaw error (in-plane angular error, $\Delta\alpha$) smaller than $\pm 1.5^\circ$ allows achieving the $\Delta L <$ 1-dB criterion. Due to limitations in our setup, the pitch angle study was bounded to 0.45°. A $\Delta L < 1$ dB was achieved for all angles and all frequencies up to 110 GHz. According to our simulations, the appearance of higher-order modes limits each axis and each angle tolerances for frequencies where a multimode regime is possible for the DRW, so a tradeoff between maximum working frequency and mechanical precision can be set for a measurement setup. For this DRW design, special care must be placed when aligning the probe and the landing pad axes for frequencies above 200 GHz. A tolerance study for frequencies above 110 GHz requires integrating optoelectronics sources and detectors in our system. This work is being carried out, and results will be reported in a future contribution.

IV. Conclusion

This work presents a novel high-frequency interconnection paradigm based on dielectric waveguide technology using noncontact near-field signal coupling. It covers the microwave (3–30 GHz) and the millimeter-wave (30–300 GHz) frequency bands. The presented simulations demonstrate the coupling of signals without the need for physical contact for frequencies from 50 GHz to at least 340 GHz with insertion losses below 2 dB between the two connected devices in a back-to-back setup. We extend this concept, to eliminate the lower cut-off frequency, introducing metal contacts in the structure. The resulting interconnection is no longer contactless; however, our simulation results show an operating range from 0 Hz up to 340 GHz. This is the widest operating range of an interconnection to date, replacing the current W1 coaxial connector standard (dc–110 GHz) and three rectangular waveguide standards, WR7 (110–170 GHz), WR5 (140–220 GHz), and WR3 (220–330 GHz).

This high-frequency interconnection paradigm is highly versatile, enabling a novel type of RF test probe to interface high-end test instrumentation with high-frequency devices during their development phase. This is extremely useful as devices are required to be broadband and their complexity is increasing to the point where a complete wireless system can be fitted on a single IC. A prototype of the RF test probe has been manufactured and characterized, validating the concept from 55 to 110 GHz and demonstrating insertion losses ΔL smaller than 1 dB at 110 GHz within the tolerances of ± 100 μm in the X-axis, ± 700 μm in the Y-axis, a gap between probe and landing pad up to ± 40 μm, and error angles in the pitch and yaw of 0.45° and $\pm 1.5^\circ$, respectively. A key advantage of this probe is that it is also backward compatible, being capable of interfacing with current rectangular and circular waveguide standards.

References

[1] M. J. Marcus, "Progress in opening access to spectrum above 100 GHz," *IEEE Wireless Commun.*, vol. 26, no. 2, pp. 2–3, Apr. 2019, doi: 10.1109/MWC.2019.8700131.

[2] 2022. [Online]. Available: https://docs.fcc.gov

[3] K. Sengupta, T. Nagatsuma, and D. M. Mittleman, "Terahertz integrated electronic and hybrid electronic–photonic systems," *Nature Electron.* vol. 1, pp. 622–635, 2018, doi: 10.1038/s41928-018-0173-2.

[4] C. M. Grötsch, I. Dan, L. John, S. Wagner, and I. Kallfass, "A compact 281–319 GHz low-power downconverter MMIC for superheterodyne communication receivers," *IEEE Trans. Terahertz Sci. Technol.*, vol. 11, no. 2, pp. 231–239, Mar. 2021, doi: 10.1109/TTHZ.2020.3038043.

[5] S. Nellen et al., "Experimental comparison of UTC- and PIN-photodiodes for continuous-wave terahertz generation," *J. Infrared Millimeter Terahertz Waves*, vol. 41, pp. 343–354, 2020, doi: 10.1007/s10762-019-00638-5.

[6] L. E. García-muñoz et al., "Photonic-based integrated sources and antenna arrays for broadband wireless links in terahertz communications," *Semicond. Sci. Technol.*, vol. 34, 2019, Art. no. 054001, doi: 10.1088/1361-6641/aaf8f2.

[7] A. Rumiantsev and R. Doerner, "RF probe technology: History and selected topics," *IEEE Microw. Mag.*, vol. 14, no. 7, pp. 46–58, Nov./Dec. 2013, doi: 10.1109/MMM.2013.2280241.

[8] FormFactor Probe Selection Guide, p. 18, 2022. [Online]. Available: https://www.formfactor.com/download/probe-selection-guide/?wpdmdl=2561&refresh=62402327e32bf1648370471

[9] Anritsu Corporation, New VNA technologies enable millimeter-wave broadband testing to 220 GHz, White Paper, 2020.

[10] H. J. Song, "Packages for Terahertz Electronics," *Proc. IEEE*, vol. 105, no. 6, pp. 1121–1138, Jun. 2017, doi: 10.1109/JPROC.2016.2633547.
[11] L. Chen et al., "Terahertz micromachined on-wafer probes: Repeatability and reliability," *IEEE Trans. Microw. Theory Techn.*, vol. 60, no. 9, pp. 2894–2902, Sep. 2012, doi: 10.1109/TMTT.2012.2205016.
[12] M. Seelmann-Eggebert et al., "On the accurate measurement and calibration of S-parameters for millimeter wavelengths and beyond," *IEEE Trans. Microw. Theory Techn.*, vol. 63, no. 7, pp. 2335–2342, Jul. 2015, doi: 10.1109/TMTT.2015.2436919.
[13] D. F. Williams et al., "Crosstalk corrections for coplanar-waveguide scattering-parameter calibrations," *IEEE Trans. Microw. Theory Techn.*, vol. 62, no. 8, pp. 1748–1761, Aug. 2014, doi: 10.1109/TMTT.2014.2331623.
[14] G. N. Phung et al., "Influence of microwave probes on calibrated on-wafer measurements," *IEEE Trans. Microw. Theory Techn.*, vol. 67, no. 5, pp. 1892–1900, May 2019, doi: 10.1109/TMTT.2019.2903400.
[15] C. Yadav et al., "Importance and requirement of frequency band specific RF probes EM models in Sub-THz and THz measurements up to 500 GHz," *IEEE Trans. Terahertz Sci. Technol.*, vol. 10, no. 5, pp. 558–563, Sep. 2020, doi: 10.1109/TTHZ.2020.3004517.
[16] C. Caglayan, G. C. Trichopoulos, and K. Sertel, "Non-contact probes for on-wafer characterization of sub-millimeter-wave devices and integrated circuits," *IEEE Trans. Microw. Theory Techn.*, vol. 62, no. 11, pp. 2791–2801, Nov. 2014, doi: 10.1109/TMTT.2014.2356176.
[17] H. Zhu, J. Gauthier, and K. Wu, "Silicon probe measurement and characterization in sub-THz range," *IEEE Trans. Terahertz Sci. Technol.*, vol. 10, no. 6, pp. 606–616, Nov. 2020, doi: 10.1109/TTHZ.2020.3013802.
[18] A. Samir, M. Basha, A. M. Hegazy, and S. Safavi-Naeini, "A CPW excitation using a contactless dielectric waveguide probe for the V-band," in *Proc. 50th Eur. Microw. Conf.*, 2021, pp. 983–986, doi: 10.23919/EuMC48046.2021.9338115.
[19] G. Carpintero et al., "Interconnection challenges on integrated terahertz photonic systems," *Proc. SPIE*, vol. 11692, 2021, Art. no. 116920N, doi: 10.1117/12.2582982.
[20] C. H. Chandler, "An investigation of dielectric rod as wave guide," *J. Appl. Phys.*, vol. 20, pp. 1188–1192, 1949, doi: 10.1063/1.1698306.
[21] D. Lyubchenko, S. Tretyakov, and S. Dudorov, *Millimeter-Wave Waveguides*. Amsterdam, The Netherlands: Kluwer, 2003, doi: 10.1007/b105858.
[22] A. A. Generalov, D. V. Lioubtchenko, J. A. Mallat, V. Ovchinnikov, and A. V. Räisänen, "Millimeter-wave power sensor based on silicon rod waveguide," *IEEE Trans. Terahertz Sci. Technol.*, vol. 2, no. 6, pp. 623–628, Nov. 2012, doi: 10.1109/TTHZ.2012.2223111.
[23] E. Brown, F. Smith, and K. McIntosh, "Coherent millimeter-wave generation by heterodyne conversion in low-temperature-grown GaAs photoconductors," *J. Appl. Phys.*, vol. 73, no. 3, pp. 1480–1484, 1993, doi: 10.1063/1.353222.
[24] H. Ito, F. Nakajima, T. Furuta, and T. Ishibashi, "Continuous THz-wave generation using antenna-integrated uni-travelling-carrier photodiodes," *Semicond. Sci. Technol.*, vol. 20, no. 7, 2005, Art. no. S191, doi: 10.1088/0268-1242/20/7/008.
[25] G. Döhler et al., "THz-photomixer based on quasi-ballistic transport," *Semicond. Sci. Technol.*, vol. 20, no. 7, 2005, Art. no. S178, doi: 10.1088/0268-1242/20/7/007.
[26] S. Kim et al., "Ultra-wideband (From DC to 110 GHz) CPW to CPS transition," *Electron. Lett.*, vol. 38, pp. 622–623, 2002, doi: 10.1049/el:20020423.
[27] I. Ocket, M. Cauwe, and B. Nauwelaers, "Millimeter wave planar transition from plastic rectangular waveguide to 1 mm coax," in *Proc. IEEE MTT-S Int. Microw. Symp.*, 2016, pp. 1–4, doi: 10.1109/MWSYM.2016.7540251.
[28] ANSYS HFSS 19.1 Full-Wave Simulator, 2022.
[29] C. Kolb, "BN 533402 - PCB-Launch connector 1.0 mm socket," Spinner GmbH, Munich, Germany, Test Rep., 2019.

Alejandro Rivera-Lavado was born in Madrid, Spain, on Oct. 24, 1984. He received the Engineering degree in telecommunications and the Ph.D. degree in communications (cum laude) from Carlos III University, Madrid, Spain, in 2010 and 2016, respectively.

Since 2018, he has been with Yebes Observatory, Dirección General del Instituto Geográfico Nacional, Yebes, Spain. His research interests include dielectric lenses, terahertz antennas, low-loss terahertz transmission lines, and radio astronomy instrumentation.

Muhsin Ali received the B.S. degree in telecommunications engineering from NUCES, Karachi, Pakistan, in 2011, the M.S. degree in electrical engineering from NUST, Islamabad, Pakistan, in 2013, and the Doctorate degree in electrical, electronics, and automation engineering from Universidad Carlos III de Madrid (UC3M), Madrid, Spain, in 2020.

In 2016, he joined UC3M as a Ph.D. Student under the MSCA-ITN project FiWiN5G. He was a Visiting Researcher with Fraunhofer Heinrich Hertz Institute, Berlin, Germany (COST EUIMWP programme), in 2019, and the University of Duisburg-Essen, Duisburg, Germany, in 2021. Since 2020, he has been a Research Fellow with UC3M under the EU-funded projects TERAWAY and TERAmeasure where he focuses on designing THz dielectric waveguides and phased array antennas for the applications of instrumentation, sensing, and wireless systems. He has authored and coauthored a book chapter, 6 peer-reviewed journal publications, and more than 20 conference papers. He has delivered two workshops at international conferences. His research interests include the design, fabrication, and integration aspects of mmWave and THz photonic emitters and electronic detectors for high-speed wireless links with beam-steering capability aimed at beyond 5G systems.

Dr. Ali is a Guest Editor of *Photonics* journal.

Daniel Gallego-Cabo received the B.S. degree in physics and the M.S. degree in optoelectronics from the Universidad de Santiago de Compostela, Santiago, Spain, in 2003, and the Ph.D. degree in electrical, electronics, and automation engineering from Universidad Carlos III de Madrid (UC3M), Madrid, Spain, in 2016.

He is currently a Research Fellow with UC3M under the EU-funded TERAmeasure project where he focuses on the characterization of THz dielectric waveguides and THz probes for instrumentation and sensing applications. His research interests include high-power short-pulse diode laser instrumentation, optical fiber sensors, optical detection and generation of high-frequency ultrasounds, and optoacoustic imaging systems for biomedical applications.

Luis-Enrique García-Muñoz received the Electrical Engineering and Ph.D. degrees from the Universidad Politecnica de Madrid (UPM), Madrid, Spain, in 1999 and 2003, respectively.

He is currently a Full Professor with Universidad Carlos III de Madrid, Madrid, Spain. He has managed or participated in several national and European research projects in areas, such as antennas and microwave receivers. He has coauthored 68 papers in international journals and holds 4 patents. His current research interests include mm and sub-mm antennas, radio astronomy instrumentation, radiometers, and quantum electrodynamics.

Dmitri V. Lioubtchenko (Member, IEEE) was born in Gorky, Russia, in May 1971. He received the B.S., M.S., and Ph.D. degrees in applied physics and mathematics from the Department of Physical and Quantum Electronics, Moscow Institute of Physics and Technology, Moscow, Russia, in 1993, 1994, and 1998, respectively.

From 1994 to 1997, he was a Researcher with the Institute of Radioengineering and Electronics, Russian Academy of Sciences, Moscow. From 1997 to 1998, he was a Visiting Postdoctoral Researcher with The University of Liverpool, Liverpool, U.K. In 1998, he joined the Radio Laboratory, Helsinki University of Technology, now Aalto University, Finland, where he has been a Docent since 2005. In 2017, he received a Docentship with the Department of Micro and Nano Science, KTH, Sweden. Since 2019, he has been a Full Professor with the Institute of High-Pressure Physics, Polish Academy of Science. He was a Visiting Researcher with The University of Liverpool (1997–1998, 2003), Trinity College, University of Dublin, Ireland (2001), Chalmers University of Technology, Sweden (MC2 access program for use of clean room, supported by EU, 2008), and Universidad Carlos III de Madrid (COST VISTA program, 2014). He has more than 25 years of experience in electrical engineering, especially in the development of new materials for millimeter, microwave, and optoelectronic applications, particularly, in the development of active and passive dielectric waveguides and components for the frequency above 100 GHz. He has authored or coauthored more than 120 papers in refereed books, journals, and conferences. He is also an author of two monographs on millimeter wave components and on dielectric rod waveguides and resonators.

Dr. Lioubtchenko was a Finnish Academy Research Fellow from 2008 till 2013. He is a member of the EuMA General Assembly (GA) from January 2016 to December 2018.

Guillermo Carpintero (Senior Member, IEEE) received the Telecommunication Engineering degree from the Universidad Politécnica de Madrid (UPM), Madrid, Spain, 1994, and the Ph.D. degree from Universidad Carlos III de Madrid (UC3M), Madrid, in 1999.

He is currently a Professor with the Electronics Technology Department, UC3M, and the Co-Director of the Optoelectronics and Laser Technology Group (GOTL). He has participated in technical program committees of numerous scientific conferences (ECOC, IRMMW-THz, MWP). His research interests include integrated microwave photonics, hybrid photonic integration, integrated mode-locked lasers, photonic-enabled beam-steered array antennas, integrated Terahertz technology, and high-frequency packaging.

Prof. Carpintero research outcome was recognized with several research awards and distinctions, including the “doctoral thesis extraordinary award” from UC3M in 2000, “HeatherWilliamsonYoung Investigator Award” from International Society for Optics and Photonics in 2000, UC3M Social Council Excellence Award in 2009, and 2011 Best European R&D Project in Cooperation Award from Madri+d Foundation.